ChemComm

Accepted Manuscript

ROYAL SOCIETY OF CHEMISTRY

rsc.li/chemcomm

View Article Online
DOI: 10.1039/C9CC02194A

COMMUNICATION

Mechanism of structural changes and crystallization kinetics of amorphous red phosphorus to black phosphorus under high pressure

Received 00th January 20xx,
Accepted 00th January 20xx

DOI: 10.1039/x0xx00000x

Heng Xiang,[a,c] Yuting Nie,[c] Hechuang Zheng,[c] Xuhui Sun,[*c,d] Xueliang Sun,[*b,d] and Yang Song,[*a,d]

The pressure-induced crystallization of amorphous red phosphorus to black phosphorus was investigated by in situ Raman spectroscopy and high resolution transmission electron microscopy. Raman measurements revealed slow crystallization kinetics. Morphology and crystal structural analysis provide detailed information on nucleation and crystal growth as well as the crystallization mechanism.

Black phosphorus (BP) is a reviving material used in a wide range of applications such as transistors, batteries, solar cells, photodetectors, photocatalysts, thermoelectric and biomedical devices.[1-7] Bulk BP is generally synthesized from white phosphorus or mostly amorphous red phosphorus (ARP) as precursors.[3,6,7] As an important thermodynamic parameter, pressure not only facilitates the synthesis of BP,[3, 7] but also plays a highly efficient role in tuning the structures and properties of BP. At ambient conditions, BP crystalizes into an orthorhombic lattice (A17, space group *Cmce, Z*=8)[8] with a graphene-like but puckered layer structure (Figure S1, ESI). It undergoes two reversible structural transitions when subject to compression to 60 GPa at room temperature.[8] The first phase transition takes place at about 5.5 GPa, from orthorhombic (A17) to rhombohedral (A7, space group $R\bar{3}m$, Z=2)[8] structure (Figure S1, ESI). At 10 GPa the second phase transition occurs from A7 to simple-cubic phase (space group $Pm\bar{3}m$, Z=1)[8] with non-layered metallic structure(Figure S1, ESI). From synthetic point of view, the structures of ARP under pressure have also been extensively investigated by Raman spectroscopy and in situ X-ray diffraction. [9-11] Under ambient conditions, ARP is a medium-range-order semiconductor[10] consisting of various subunits in a polymeric network. These subunits exist in many forms, for example, as shown in Fig. 1 c and d, P_3 triangles and P_4 pyramidal structures linked by chains of P atoms[10], P_2 connected P_8 and P_9 cages as in type IV and V crystalline red phosphorus[7, 12] (Fig. 1 c), and other different units presented in type II crystalline red phosphorus[13, 14] (Figure S1, ESI). These structures can be substantially altered upon compression, including the change average P-P-P angles[10] and dramatic volume collapse that ultimately leads to the formation of crystalline BP. [8, 11]

Despite the extensive high-pressure studies on both BP and ARP that established various high-pressure polymorphic structures, the nature of the pressure-induced crystallization from ARP to BP remains unclear. Understanding the mechanism of amorphous-to-crystalline structural evolution at microscopic level is of fundamental importance in the controlled synthesis and subsequent applications of BP. In this communication, we use time-dependent in situ Raman spectroscopy combined with high-resolution transmission electron microscopy (HRTEM) to characterize the crystallization process from ARP to BP. Our data provide new crystallization kinetics and reveal the untraditional growth mechanism involving stress-driven structural rearrangement and oriented attachment. This work provides additional insight into understanding the ARP to BP transformation process.

At room temperature, previous studies suggest the ARP can transform into BP in the pressure range from 5.5 to 8.0 GPa. [8, 9, 11, 15] Therefore, we monitored the transition process by compressing ARP in a diamond anvil cell using in situ Raman spectroscopy with selected spectra shown in Fig. 1a. At near ambient pressure (e.g., 0.07 GPa), the Raman profile shows characteristic ARP bands. For instance, the peak at 352 cm^{-1} is assigned to B fundamental mode, whereas the doublets at 389-399 cm^{-1} and 454-462 cm^{-1} are associated with an A_1 symmetric stretch motion and E degenerate mode, respectively.[11] Peaks below 400 cm^{-1} are related to the P_8 and P_9 structures, while the

[a] Department of Chemistry, University of Western Ontario, London, Ontario N6A 5B7, Canada. Email: yang.song@uwo.ca
[b] Department of Mechanical and Materials Engineering, University of Western Ontario, London, Ontario N6A 5B9, Canada.
[c] Institute of Functional Nano and Soft Materials (FUNSOM), and Jiangsu Key Laboratory for Carbon-based Functional Materials and Devices, Soochow University, Suzhou, Jiangsu 215123, P. R. China.
[d] Soochow University -Western University Centre (SWC) for Synchrotron Radiation Research, Western University, London ON N6A 5B7 Canada.
† Footnotes relating to the title and/or authors should appear here.
Electronic Supplementary Information (ESI) available: [details of any supplementary information available should be included here]. See DOI: 10.1039/x0xx00000x

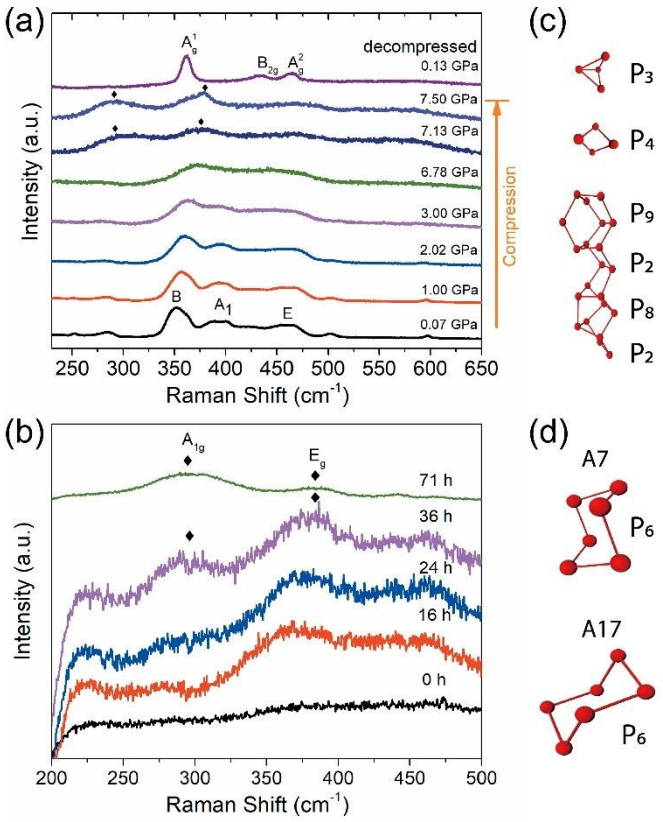

Fig. 1 (a) *In-situ* high-pressure Raman spectra of compression up to7.50 GPa and decompression at 0.13 GPa. At 7.13 GPa two new weak and broad peaks, labeled by black diamonds, suggest the formation of crystalline BP in A7 phase. (b) The time-dependent Raman spectrum of compressed ARP at the pressure of 6.76 GPa for 0, 16, 24, 36, and 71 hours. The two small and broad peaks (labeled with black diamonds) centered at 290 cm^{-1} and 378 cm^{-1}, respectively, appear at 36 and 71 hours, indicating the A7 phase of BP as in (a) at a pressure above 7 GPa. (c) P_3, P_4, P_2 and P_9 subunits of ARP, and (d) different P6 ring structures in A17 and A7 phases of BP.

small peak at 598 cm^{-1} is the A_1 symmetric stretch of P_4 structure (Fig. 1c) [11] Although all Raman active modes were weakened as the pressure increased up to 3.00 GPa as the result of band gap closing[10] and deformation of structural subunits by compression, the peak positions showed a weak pressure dependence (Figure S2, ESI). Among all Raman active modes, B mode shows the largest redshift but less than 3 $cm^{-1}GPa^{-1}$, suggesting that pressure has insignificant influence in the local bonds. The redshift of B mode was believed to be associated with the decrease of vibrational interaction between subunits during volume contraction under high pressure.[10] Subsequent compression to pressure higher than 3.00 GPa can force connected P_3 and/or P_4 subunits to separate and buckle into surrounding space.[10] Above 5 GPa, indeed, these deformed chain-linked subunits stiffen significantly as suggested by the broad Raman profiles until crystallization at 7.13 GPa into the A7 phase of BP evidenced by observation of the two weak Raman peaks at 290 cm^{-1} and 378 cm^{-1} labeled by black diamonds (Fig. 1a).[9] These two peaks became more prominent upon further compression up to 7.50 GPa, suggesting the increased crystallinity of the A7 phase. When the pressure is relieved, the A7 phase transforms into the A17 phase evidenced by three sharp peaks observed in the Raman spectrum of the recovered sample (Figure 1a).[9, 11] This observation is consistent with previous report where the phase transition is reversible upon compression and decompression.[8, 11, 16] In the transition region, these two crystalline phases of BP are composed of different six-membered rings (Fig. 1d), and they coexist at the pressure range from about 5 GPa and to 7.5 GPa,[11, 16] which coincidently overlaps with the crystallization of ARP to BP in A7 phase. These phase transition sequences are illustrated in a schematic phase diagram (Figure S3a, ESI).

To deconvolute this complexity to reveal the origin of crystallization of ARP to BP, we focused on the pressure region between 6.78 GPa and 7.13 GPa by performing time-dependent Raman spectroscopy. Specifically, additional high-pressure experiments were carried out by setting the maximum compressing pressure at 6.76 GPa followed by Raman measurement as a function of time. As shown in Fig. 1b and in a schematic diagram (Figure S3b, ESI), the spectrum at this pressure presents no features of either ARP or BP in the first 24 hours. After 36 hours, two new broad peaks (labeled by black diamonds) centered at 290 cm^{-1} and 378 cm^{-1} appeared, corresponding to the A_{1g} and E_g modes, respectively, of the A7 phase of BP.[9] As the dwelling time prolonged to 71 hours, this crystalline phase became more prominent and can be compared with the phase under 7.5 GPa in Raman spectra of Fig. 1a. These results suggest that the crystallization kinetics of ARP is sluggish at 6.76 GPa but can be accelerated at higher pressures as demonstrated by the regular Raman measurements as a function of pressure in this study. On the other hand, however, the slow crystallization process of ARP at this pressure allows the detailed studies of the transition process from the nanostructure perspective by pressure quenching as discussed below.

Correspondingly, an extra ARP sample was pressurized and allowed dwelling at 6.76 GPa for 36 hours, then reclaimed and prepared for HRTEM characterizations (Figure S4, ESI). As shown in Fig. 2a, the small crystalline domains distinguish from the amorphous matrix, consistent with the partial crystallization of ARP observed in Raman measurements. These domains are less than 5 nm in diameter on average and thus suggest the initiation of nucleation at the fixed pressure of 6.76 GPa. The nucleation site (Fig. 2b) exhibit oriented lattices, with lattice fringes of 2.1 Å corresponding to (131) plane of the A17 phase of BP. However, the atomic arrangement in the nucleation site is structurally inferior to either few-layer BP[17] or BP quantum dots[18]. In particular, some sites exhibit similar lattice fringes but different orientations (Fig. 2 b and c), eventually leading to the formation of crystal twinning in a product (Figure S5, ESI). In addition to the well-developed crystalline nucleation sites, some small domains are characterized by partially ordered atomic arrays with crystalline lattice feature of aligned arrangement but largely amorphous in nature (Fig. 2d). As shown in the highlighted area in Fig. 2d, such domains are believed to be the precursors of the nucleation sites. That is, upon further compression or longer dwelling time at this pressure, these quasi lattices are expected to transform into the corresponding crystalline lattice completely.

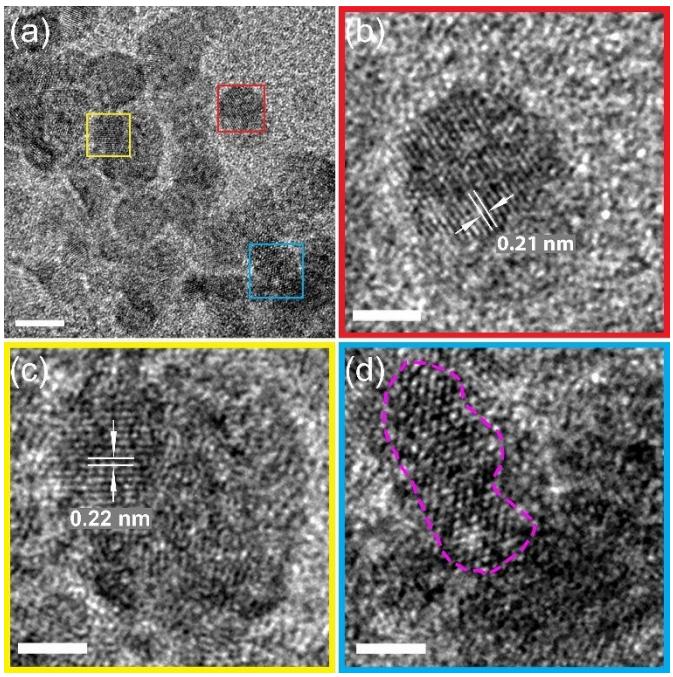

Fig. 3 HRTEM images of structures of nucleation sites in the reclaimed sample from 6.76 GPa dwelled for 36 hours. (a) multiple nucleation sites distributed in ARP matrix as the result of pressure-induced nucleation. The red, yellow and blue squares marked sites are shown in (b), (c) and (d), respectively in detail. In (b) and (c), two crystallization domains show similar lattice fringes of 0.21 nm and 0.22 nm corresponding to [131] and [002] planes of A17 phases, respectively. (d) The atomic order in the area highlighted by dashed pink line shows the very beginning of lattice formation. At the edge of (c) and in (d), structures of subunits are clearly different from amorphous matrix, indicating atomic rearrangement at high pressure. The scale bars are 5 nm in (a) and 2 nm in (b), (c) and (d).

For the formation of the nucleation sites from amorphous state, the driving force can be understood from both macroscopic and microscopic models. Macroscopically, homogeneous nucleation process in the amorphous matrix can be described by the Gibbs free energy change of the system[19]

$$\Delta G(T,P) = \frac{(1/6)\pi d^3}{V^c}\left(\Delta G^{am\to c} + E\right) + \pi d^2\sigma + P\Delta V$$

where d is the diameter of a crystalline nucleus, $\Delta G^{am\to c}$ is the molar free energy change for amorphous to crystalline transformation, σ is the free energy increase for forming the unit area of crystalline/amorphous interface, $V^c$is the molar volume of crystalline phase, ΔV is the volume change during the formation of the crystal nucleus, and E is the elastic energy induced by the volume change. Generally, E can be omitted because of its minor impact on the free energy change during the nucleation.[19] Considering minor pressure dependence of other terms, therefore, it can be deduced the volume change due to applied pressure constitutes the governing factor in nucleation process. Indeed, previous experiment suggests that the transformation of amorphous to A7 phase is accompanied by a substantial volume collapse of at least 10%.[11] Microscopically, structural rearrangement of subunit in favor of the formation of P_6 configuration must occur concurrently with the pressure-induced nucleation process. In particular, Zaug et al. showed that structural rearrangement occurred prior to crystallization via the reduction of the average P-P-P angle of ARP upon compression. [10] As a result, structural rearrangement involving the change of bond angles and reorientations of the subunits allows the emergence of quasi lattices (Fig. 2d) which subsequently transform into lattice (Fig. 2b and c). Ideally, these processes involving structural evolution of short- and intermediate-range subunits can be better understood from time-resolved *in-situ* high-energy X-ray scattering.

Upon successful nucleation, subsequent crystalline growth is the other important step for the effective conversion of ARP to BP. During the growth process, crystalline domains expand into the amorphous matrix, where the crystalline/amorphous interface provides rich information about the growth mechanism. As shown in a representative HRTEM image (Fig. 3a), three distinctive regions with different degree of ordered structures can be observed, i.e., the amorphous region(I), crystalline region (II), and an intermediate region (III). The amorphous region features completely disordered structures (Figure S6, ESI), whereas the crystalline region can be characterized by the well-defined lattice fringes of 0.34 nm and

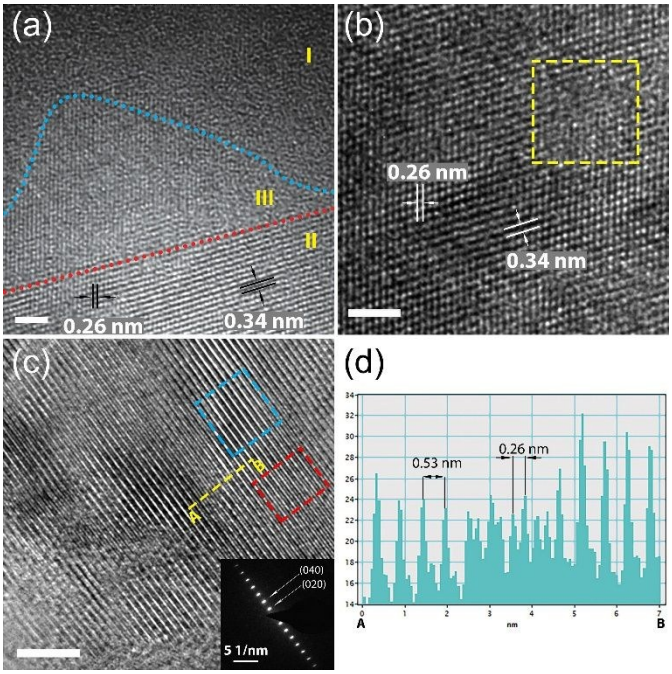

Fig. 2 HRTEM images of structures of crystalline-amorphous hybrid and crystallite in the reclaimed sample from 6.76 GPa dwelled for 36 hours. (a) The dotted blue and red lines indicate the boundaries among three regions: amorphous (region I), crystalline (region II), and intermediate (region III). (b) An assembly of rearranged subunits, highlighted by dashed yellow square, attached onto the {100} crystalline plane during the crystal growth. In both (a) and (b), the lattice fringes are 0.26 nm and 0.34 nm, corresponding to (040) and (021) plane, respectively. (c) The formed crystallite shows apparent lattices of (020) and (040) planes, corresponding to lattice fringes of 0.26 nm and 0.53 nm, respectively. Missing atoms in (040) planes were found in areas labeled by blue square compared to area in dashed red square. The inset shows SEAD pattern of the area in dashed red square. (d) An intensity profile was scanned along line from A to B.

0.26 nm, corresponding to (040) and (021) planes of A17 phase, respectively. Interestingly, the intermediate region was found amorphous in nature (Figure S7, ESI). The formation of intermediate region can be understood from the deviatoric stress driven re-orientation of the nanocrystalline domains.[20]

Under the uniaxial compression condition, anisotropic stress strongly facilitates the rearranged subunits align along a commonly preferred crystallographic orientations coalescing neighbor subunits, distinguishing the semi-ordered structures from the remaining amorphous domains, forming the I-III boundary. However, their orientations might be slightly different from the (040) and (021) crystalline planes in the well-developed crystalline region (II). Upon further stress, oriented attachment via the energetically favorably facets (040 and 021 in this case) is expected to promote the expansion of crystalline region II into the intermediate region III. Such stress-induced oriented attachment model is further manifested on different crystal planes, e.g., {100} planes (Fig. 3b). A few rearranged subunits (dashed square region) with matching local lattice are preferentially attached on the {100} crystalline plane, leading to the crystal growth on top the existing crystalline plane.

Overall, this crystal growth mechanism is different from conventional crystallization theory, [20] where the crystal growth is described by ion-by-ion attachment which is often limited by diffusion and other constraints. Such oriented attachment mechanism has been proposed to interpret the pressure-induced crystalline growth from nanoparticles, analogous to our study here. [20-23] Under this model, rearranged subunits with matching crystallographic orientations of the crystalline phase will be bridged in priority under applied stress. As a result, other subunits with mismatching crystallographic orientations will highly likely give rise to the defects such as vacancies. Indeed, careful examination of formed crystalline planes under HRTEM shows that large amount of atomic vacancies are formed on the crystalline surface as shown in Fig. 3c. As can been seen, the normal lattice in the red box is featured with (040) and (020) planes, but (040) is mostly missing in the blue boxed region. A linear intensity profile (Fig. 3d) scanned along the dashed yellow line AB in Fig. 3c shows the distribution of lattice fringes of 0.53 Å and 0.26 Å, indicating substantial atomic vacancies, consistent with the oriented attachment model.

In summary, we examined crystallization process from ARP to BP using Raman spectroscopy and HRTEM. Raman results show that crystallization process has a pressure-dependent slow crystallization kinetics. The quenched partially crystallized samples allow detailed morphology and structural analysis using HRTEM. At threshold of crystallization, nucleation from amorphous matrix is driven by pressure-induced volume collapse and structural rearrangement of the subunits. TEM images show three representative regions of different orderness. The intermediate phase is amorphous in nature but can undergo a facile conversion into crystalline phase via oriented attachment. This unconventional crystallization mechanism is correlated with stress driven structural rearrangement and re-orientation from nanocrystalline nucleation sites. Our findings elucidate the crystallization process of ARP to BP at atomic level and thus contributes to the fabrication of specifically structured BP for further applications.

We acknowledge the Natural Science and Engineering Research Council of Canada (NSERC) for Discovery Grants (X.S. and Y.S.), and a Leading Opportunity Fund from the Canadian Foundation for Innovation (Y.S.). The work was also supported by China National Key R&D Program (Grant No. 2017YFA0205002), Collaborative Innovation Center of Suzhou Nano Science & Technology, the Priority Academic Program Development of Jiangsu Higher Education Institutions (PAPD), the 111 Project, Joint International Research Laboratory of Carbon-Based Functional Materials and Devices.

Conflicts of interest

There are no conflicts to declare.

Notes and references

1 L. Li, Y. Yu, G. J. Ye, Q. Ge, X. Ou, H. Wu, D. Feng, X. H. Chen and Y. Zhang, *Nat. Nanotechnol.* , 2014, **9**, 372.
2 X. Ling, H. Wang, S. Huang, F. Xia and M. S. Dresselhaus, *Proc Natl. Acad. Sci. USA*, 2015, **112**, 4523-4530.
3 H. Liu, Y. Du, Y. Deng and P. D. Ye, *Chem. Soc. Rev.* , 2015, **44**, 2732-2743.
4 M. Batmunkh, M. Bat-Erdene and J. G. Shapter, *Adv. Mater.* , 2016, **28**, 8586-8617.
5 A. Carvalho, M. Wang, X. Zhu, A. S. Rodin, H. Su and A. H. Castro Neto, *Nat Rev Mater.*, 2016, **1**, 16061.
6 V. Eswaraiah, Q. Zeng, Y. Long and Z. Liu, *Small*, 2016, **12**, 3480-3502.
7 R. Gusmão, Z. Sofer and M. Pumera, *Angew. Chem. Int. Ed.* , 2017, **56**, 8052-8072.
8 D. Scelta, A. Baldassarre, M. Serrano-Ruiz, K. Dziubek, A. B. Cairns, M. Peruzzini, R. Bini and M. Ceppatelli, *Chem. Commun.* , 2018, **54**, 10554-10557.
9 Y. Akahama, M. Kobayashi and H. Kawamura, *Solid State Commun.* , 1997, **104**, 311-315.
10 J. M. Zaug, A. K. Soper and S. M. Clark, *Nat. Mater.* , 2008, **7**, 890.
11 E. N. Rissi, E. Soignard, K. A. McKiernan, C. J. Benmore and J. L. Yarger, *Solid State Commun.* , 2012, **152**, 390-394.
12 J. B. Smith, D. Hagaman, D. DiGuiseppi, R. Schweitzer-Stenner and H.-F. Ji, *Angew. Chem. Int. Ed.* , 2016, **55**, 11829-11833.
13 P. Arno, B. M. F., Z. Josef, B. Gunther and E. Hellmut, *Angew. Chem. Int. Ed.* , 2004, **43**, 4228-4231.
14 R. A. L. Winchester, M. Whitby and M. S. P. Shaffer, *Angew. Chem. Int. Ed.* , 2009, **48**, 3616-3621.
15 J. C. Jamieson, *Science*, 1963, **139**, 1291-1292.
16 S. E. Boulfelfel, G. Seifert, Y. Grin and S. Leoni, *Phys. Rev. B*, 2012, **85**, 014110.
17 J. R. Brent, N. Savjani, E. A. Lewis, S. J. Haigh, D. J. Lewis and P. O'Brien, *Chem. Commun.* , 2014, **50**, 13338-13341.
18 Y.-J. Yuan, S. Yang, P. Wang, Y. Yang, Z. Li, D. Chen, Z.-T. Yu and Z.-G. Zou, *Chem. Commun.* , 2018, **54**, 960-963.
19 F. Ye and K. Lu, *Phys. Rev. B*, 1999, **60**, 7018-7024.
20 Z. Wang, C. Schliehe, T. Wang, Y. Nagaoka, Y. C. Cao, W. A. Bassett, H. Wu, H. Fan and H. Weller, *J. Am. Chem. Soc.* , 2011, **133**, 14484-14487.
21 D. Li, M. H. Nielsen, J. R. I. Lee, C. Frandsen, J. F. Banfield and J. J. De Yoreo, *Science*, 2012, **336**, 1014-1018.
22 H. Wu, Z. Wang and H. Fan, *J. Am. Chem. Soc.* , 2014, **136**, 7634-7636.
23 J. J. De Yoreo, P. U. P. A. Gilbert, N. A. J. M. Sommerdijk, R. L. Penn, S. Whitelam, D. Joester, H. Zhang, J. D. Rimer, A.

Navrotsky, J. F. Banfield, A. F. Wallace, F. M. Michel, F. C. Meldrum, H. Cölfen and P. M. Dove, *Science*, 2015, **349**, aaa6760.

View Article Online
DOI: 10.1039/C9CC02194A

View Article Online
DOI: 10.1039/C9CC02194A

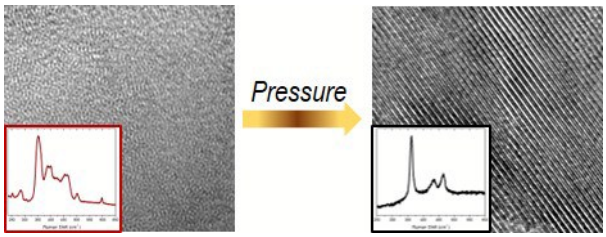

Revealing untraditional crystallization mechanism of amorphous red phosphorus to black phosphorus under high pressure.